Anatomy of spin Hall and anomalous Hall conductivities in Co/5*d*-heavy-metal heterostructures from band filling and interfacial orbital hybridization

Kenji Nawa,[1,2,*] Mana Fukutani,[1] and Kohji Nakamura[1]
[1]*Graduate School of Engineering, Mie University, Tsu, Mie 514-8507, Japan*
[2]*Research Center for Magnetic and Spintronic Materials, National Institute for Materials Science (NIMS), Tsukuba, Ibaraki 305-0047, Japan*

(Received 31 March 2023; revised 11 October 2023; accepted 7 December 2023; published 12 January 2024)

Intrinsic spin Hall and anomalous Hall conductivities (SHC and AHC) for heterostructures of Co and 5*d* heavy metal (HM = Ta, W, Re, Os, Ir, Pt) are investigated by comparing chemical (HM element) trend and different HM thickness by means of first-principles calculations. We find that the HM-element dependencies of SHC and AHC are caused by the 5*d* band filling but importantly originated from different band characteristic. The SHC associates with the spin Berry curvature in 5*d* bands inside the HM atomic layers. In contrast, the AHC is induced by the interfacial bands at the Co/HM, in which the origin can be decomposed into two effects; the 5*d* band filling of interfacial HM atomic layer and a proximity effect of neighboring Co atomic layer inducing the magnetic moment at the top HM. The former determines the overall distribution of Berry curvature in Brillouin zone, while the latter, asymmetric distribution of Berry curvature by a time-reversal symmetry breaking. As a consequence, different thickness dependencies of the HM atomic layers to the SHC and AHC appear, being significant and absent, respectively. The findings provide guiding principles for controllable SHC and AHC in device developments.

DOI: 10.1103/PhysRevMaterials.8.014405

I. INTRODUCTION

Spin-orbit-coupling (SOC)-induced phenomena have been widely reported in the past decades as the SOC enriches magnetic properties, including proximity-induced magnetic moment [1–3], perpendicular magnetocrystalline anisotropy (PMA) [4–8], Dzyaloshinskii-Moriya interaction [9,10], and spin-orbit torque (SOT) [11–13]. The utilization of the SOC-induced properties thus opens a new vista in spin-orbitronics applications [14–16]. Recent interest has addressed on highly efficient conversion between charge and spin currents, in which spin-dependent Hall effects, i.e., spin Hall effect (SHE) [17–20] and anomalous Hall effect (AHE) [21–23], are central targets. In the SHE, the transverse spin current is generated from unpolarized longitudinal charge current in nonmagnetic (NM) materials, which induces the SOT for magnetization switching in magnetic random access memory (SOT-MRAM) [24,25]. In the AHE, the transverse spin-polarized charge current is generated from longitudinal charge current in ferromagnetic (FM) materials, which is, for example, applied to ultrasensitive magnetic sensors [26–29]. The SHE and AHE originate either from an intrinsic nature, associated with the band structure, or extrinsic nature, associated with the skew scattering or side jump due to impurities. A spontaneous magnetization is accompanied in the AHE [23].

Intrinsic SHE in pure bulk HM series has been intensively investigated [30–34]. From first-principles calculations, the largest spin Hall conductivity (SHC) is found in an fcc Pt, $2200\,(\hbar/e)\,\Omega^{-1}\mathrm{cm}^{-1}$, which originates from the band structures near the Fermi level at L and X points in Brillouin zone (BZ) [30]. Tanaka *et al.* have reported that the number of *d* electrons governs the sign and absolute value of the SHC in bulk HM series [31], as is confirmed in experiments [32,34]. This indicates that the *d*-band filling is a key to control. With the similar analogy to the SHC, anomalous Hall conductivity (AHC) of Fe, Co, and Ni was quantitatively predicted from theoretical calculations [35–38], 750, 480, and $-1066\,\Omega^{-1}\mathrm{cm}^{-1}$, respectively, which are in good agreement with experiments [39,40]. In order to tune the SHC and AHC, numerous efforts have been made, especially, by alloying [41–52]. For example in a β-W, Sui *et al.* [41] theoretically and Qian *et al.* [42] experimentally demonstrated the controllable SHC through rigidly shifted Fermi level of the band structure by Ta doping. For the AHC, using $L1_0$-type FePd alloy, He *et al.* [53] observed experimentally an enhancement of the AHC by doping Pt, which introduces larger SOC effect into the alloy. Recent theoretical works reported a wide range of AHC in FM alloys, where particularly giant AHC is found in a part of Heusler alloy family [48–50].

Apart from the bulk properties, recent efforts have paid to the SHC and AHC in artificially multilayered structures including dependencies of constituent elements [54], film thickness [55], number of interfaces [56], and proximity-induced magnetic moments [57]. An interfacial orbital hybridization is one of the effective ways to modulate these properties, as reported for the AHC in Co/Pd multilayers [58,59] and Pt/Cr_2O_3 interface [60]. Very recently, Salemi *et al.* performed quantitative first-principles calculations for Pt and 3*d*-FM bilayers [61], and found that the SHC dedicates to exciting the SOT in the Pt layer. Since SHC and AHC are basic properties involved not only in SOT phenomenon but

*nawa@elec.mie-u.ac.jp

 ©2024 American Physical Society

TABLE I. Stacking structure, in-plane lattice constant (a), and interfacial distance ($d_{\rm int}$) for Co/HM$_n$ (HM = Ta, W, Re, Os, Ir, Pt; $n = 6 \sim 15$).

	Ta	W	Re	Os	Ir	Pt
Stacking	bcc	bcc	fcc	fcc	fcc	fcc
a (Å)	2.862	2.752	2.775	2.735	2.746	2.816
$d_{\rm int}$ (Å)[a]	1.97	1.99	2.02	2.04	2.03	2.00

[a]The values for $n = 15$ are shown as an example. It is confirmed that the $d_{\rm int}$s in the other n are almost identical to that in $n = 15$ within ± 0.03 Å regardless of the HM elements.

also in the anomalous Nernst effect and the recently-proposed spin anomalous Hall effect [47,62,63], elucidation of physical origin of these phenomena, especially at the interface between FM and HM, is desired for future applications.

Herein, we perform first-principles calculations for in-depth investigations of SHC and AHC in heterostructures of various 5d HM and 3d FM Co. It is found that the 5d-band filling is a key in determining sign and scale of both the SHC and AHC, where importantly the former originates from bands associated with the inside HM atomic layers and the latter is from bands at the Co/HM interfaces. The paper is organized as follows. The geometries of heterostructures and computational details are given in Sec. II. In Sec. III, results for SHC (in Sec. III A) and AHC (in Sec. III B) are presented by comparing the dependencies of HM element, its thickness, and Fermi-level shifting, and we discuss physical origins in terms of (spin) Berry curvature. Summary is finally given in Sec. IV.

II. MODEL AND METHOD

A heterostructure was modeled by a single-slab geometry, i.e., film, consisting of one monolayer (1ML) Co on nML 5d HM, where HM of Ta, W, Re, Os, Ir, and Pt across the periodic table are considered with changing the number of atomic layers, n, as 6, 9, 12, and 15. We assume a bcc structure for Ta and W where Co is stacked on the bcc(110) ($\cdots ABABAB \cdots$ stacking) and an fcc structure for Re, Os, Ir, and Pt where Co is stacked on the fcc(111) ($\cdots ABCABC \cdots$ stacking) to minimize the lattice mismatch between the Co and HM, as shown in Figs. 1(a) and 1(b). The two-dimensional (2D) BZs for these heterostructures with corresponding 3D BZs are illustrated in Figs. 1(c) and 1(d). In-plane lattice constant a was fixed to that of the bulk HM, which was obtained from the total energy calculations. The geometric parameters are summarized in Table I.

Density-functional theory (DFT) calculations were performed by means of all-electron full-potential linearized augmented plane wave (FLAPW) method [64–66] within generalized gradient approximation [67]. The LAPW basis set has a cutoff of $|\mathbf{k}+\mathbf{G}| \leqslant 3.9\,\text{a.u.}^{-1}$, and muffin-tin (MT) sphere radii are set to $2.20\,a_{\rm B}$ for Co and $2.45\,a_{\rm B}$ for HM atoms. The angular momentum expansion was truncated at $\ell = 8$. The 2D BZ was sampled by a special $\mathbf{k}$-point mesh of 15×15 for self-consistent field (SCF) calculations including atomic relaxation with the convergence criterion of atomic force, 0.005 htr/Å [68]. The interfacial distances between the

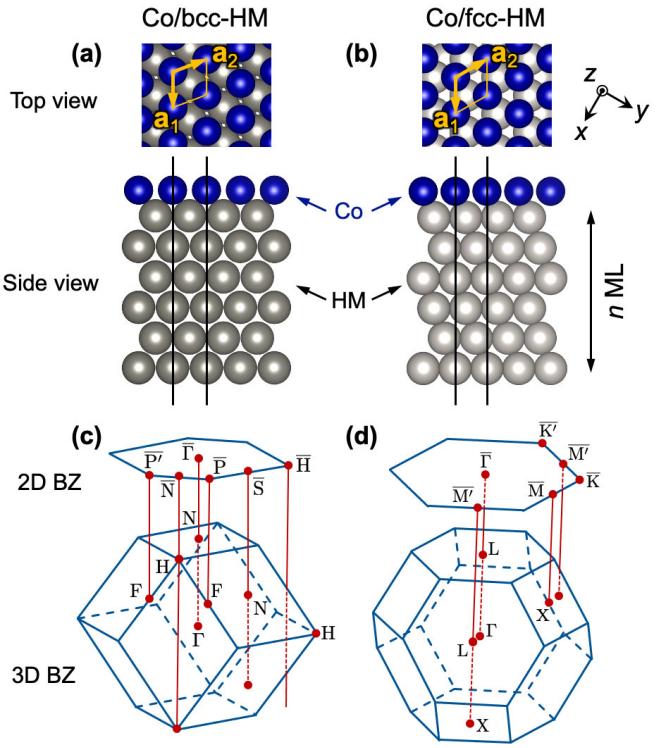

FIG. 1. Top and side views of geometry of Co ML on HM$_n$ in (a) bcc (HM = Ta, W) and (b) fcc (HM = Re, Os, Ir, Pt) stacking structures, where the number of HM atomic layers varies as $n = 6$, 9, 12, and 15 ($n = 6$ in figures). Vertical solid (black) line indicates an unit cell where semi-infinite vacuum region is involved at top and bottom sides of the slab model. (c) 2D BZ of bcc(110) plane and 3D BZ of bulk bcc and (d) those of fcc(111) plane and bulk fcc.

Co and HM after the relaxation are also given in Table I. The SOC is taken into account on the basis of second variational method [66,69,70].

We consider the spin-current flow along x direction as a response of electric field along y direction and evaluate the intrinsic SHC and AHC, $\sigma^{\rm S}_{xy}$ and $\sigma^{\rm A}_{xy}$, on the basis of the linear-response Kubo formula at the static limit, given as

$$\sigma^{\alpha}_{xy} = -\frac{e^2}{\hbar A}\sum_{\mathbf{k}}\Omega^{\alpha}_{xy}(\mathbf{k}), \tag{1}$$

where e is the elementary charge, $\hbar$ is the reduced Plank constant, and A is the unit area. Thus, the unit of SHC and AHC is given as Ω^{-1} [71–73] in SI units. This is different from the 3D system case ($\Omega^{-1}\text{cm}^{-1}$) by a factor of slab length along z-axis $d_{\rm slab}$ (the $d_{\rm slab}$ is explicitly defined in Appendix), where A is replaced with the volume of unit cell V in Eq. (1). (The results are presented in 2D unit in the main text, while those in 3D unit are given in Appendix for the sake of clarity.) A contribution of (spin) Berry curvature up to the Fermi level is written as

$$\Omega^{\alpha}_{xy}(\mathbf{k}) = \sum_{n\neq n'}(f_{\mathbf{k}n} - f_{\mathbf{k}n'})\frac{\text{Im}\langle\mathbf{k}n|\hat{v}^{\alpha}_{x}|\mathbf{k}n'\rangle\langle\mathbf{k}n'|\hat{v}_{y}|\mathbf{k}n\rangle}{(\varepsilon_{\mathbf{k}n} - \varepsilon_{\mathbf{k}n'})^2}, \tag{2}$$

where $f_{\mathbf{k}n}$ is the Fermi distribution function of nth band at $\mathbf{k}$ point. Here, α is S or A, denoting the SHC and AHC. $\varepsilon_{\mathbf{k}n}$

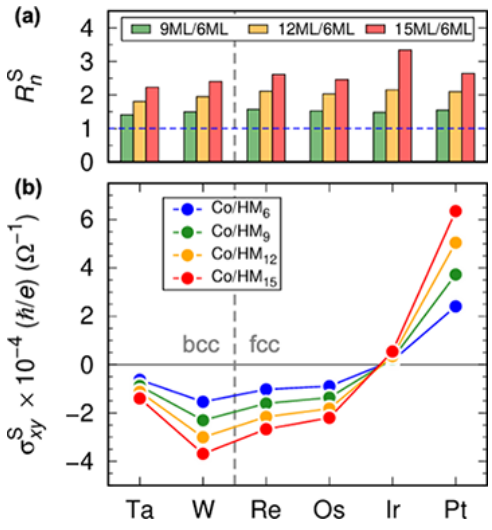

FIG. 2. (a) Change ratio of σ_{xy}^{S} against HM thickness, $R_n^S = \sigma_{xy,n}^S/\sigma_{xy,6}^S$, and (b) σ_{xy}^S for Co/HM$_n$ (HM = Ta, W, Re, Os, Ir, Pt). In (a), color bars indicate R_n^S for $n = 9$ (labelled as 9ML/6ML; green), 12 (12ML/6ML; orange), and 15 (15ML/6ML; red) with respect to $n = 6$ (blue horizontal dashed line for a reference). These colors correspond to those in (a); $n = 6$ (blue), 9 (green), 12 (orange), and 15 (red), respectively.

and $\varepsilon_{\mathbf{k}n'}$ are eigenvalues of occupied state $|\mathbf{k}n\rangle$ and unoccupied state $|\mathbf{k}n'\rangle$, respectively. An operator $\hat{v}_x^\alpha$ is spin current operator $\hat{v}_x^S \to \hat{j}_x = \frac{1}{2}(\hat{s}_z\hat{v}_x + \hat{v}_x\hat{s}_z)$ ($\hat{s}_z$ is the spin Pauli matrix) for the SHC and is velocity operator $\hat{v}_x^A \to \hat{v}_x$ for the AHC. The dense $\mathbf{k}$-point mesh of 120×120 was used for 2D full BZ integration in the SHC and AHC calculations, where numerical uncertainties were carefully tested to be minimized less than 0.1% for the SHC and 0.5% for the AHC, respectively.

III. RESULTS AND DISCUSSION

A. Spin Hall conductivity

Figure 2 shows calculated SHC (σ_{xy}^S) for the Co/HM$_n$ with varying the HM thickness of n (6, 9, 12, and 15). In Fig. 2(b), the value of σ_{xy}^S depends significantly on the HM element. For the Co/bcc-HM$_n$ (HM = Ta, W), the negative σ_{xy}^Ss are obtained and the absolute value increases as the number of $5d$ electrons increases as $\sigma_{xy}^S = -1.40\times10^{-4}$ $(\hbar/e)\,\Omega^{-1}$ in the Co/Ta$_n$ and -3.69×10^{-4} $(\hbar/e)\,\Omega^{-1}$ in the Co/W$_n$ for $n = 15$. The Co/W$_n$ shows the negative maximum value of σ_{xy}^S among the systems under study. When the number of $5d$ electrons further increases, the σ_{xy}^S in the Co/fcc-HM$_n$ increases such that for $n = 15$, $\sigma_{xy}^S = -2.67\times10^{-4}$, -2.20×10^{-4}, 0.54×10^{-4}, and 6.35×10^{-4} $(\hbar/e)\,\Omega^{-1}$ for the Co/Re$_n$, Co/Os$_n$, Co/Ir$_n$, and Co/Pt$_n$, respectively. A sign change of σ_{xy}^S occurs between the Co/Os$_n$ and Co/Ir$_n$, and the positive maximum value is found in the Co/Pt$_n$. A large increase of σ_{xy}^S in absolute value as increasing HM thickness is confirmed. To see the HM-thickness dependence more clearly, here we define a change ratio of σ_{xy}^S from the system with the thinnest HM thickness ($n = 6$), $R_n^S = \sigma_{xy,n}^S/\sigma_{xy,6}^S$, i.e., a change ratio of σ_{xy}^S in Co/HM$_n$ for $n = 9$, 12, and 15 (referred to as $\sigma_{xy,n}^S$ in this discussion) to that in Co/HM$_6$ (referred to as $\sigma_{xy,6}^S$). In Fig. 2(a), the R_n^S is proportional to the HM thickness such that the $R_n^S \sim 1.5$, 2.0, and 2.5 for $n = 9$ (green bars in figure), 12 (orange), and 15 (red). In Co/Ir$_n$ system, R_{15}^S is much higher than 2.5 due to the small value in the denominator of $\sigma_{xy,6}^S$. To argue origins of the dependencies of SHC against the HM element and the thickness, the band-filling dependencies of the σ_{xy}^S were calculated by shifting the Fermi level and presented in Fig. 3. Although they show an almost identical dependence in the Co/bcc-HM and Co/fcc-HM systems, a difference appears in the peak positions that move to lower energy as the number of $5d$ electrons increases. Moreover, in each system, the peak heights become higher for the systems of thicker HM. In the Co/bcc-HM systems, the σ_{xy}^S shows the negative peak at 1.3 eV for the Co/Ta$_n$ and at −0.6 eV for the Co/W$_n$ [see Figs. 3(a) and 3(b)]. At higher energy, the broad positive peak corresponding to the maximum σ_{xy}^S locates at 5.6 eV for the Co/Ta$_n$ and 4.5 eV for the Co/W$_n$. The Co/fcc-HM systems show the sharp peaks for both the maximum and minimum σ_{xy}^Ss at higher and lower energies, respectively [Figs. 3(c)–3(f)]. The trend of the band-filling clarifies that at zero energy, the Co/Pt$_n$ gives the largest positive value of σ_{xy}^S and then it goes to zero in the Co/Ir$_n$ while in the Co/Os$_n$, Co/Re$_n$, Co/W$_n$, and Co/Ta$_n$, it has the negative values with the largest σ_{xy}^S in the Co/W$_n$, as seen in Fig. 2(b).

To understand the spatial contribution to the SHC, by focusing on the Co/Pt$_{15}$, the energy dependence of σ_{xy}^S where the SOC effect is examined by switching on either inside Pt region or Co/Pt interface region is shown in Fig. 4(a). The inside Pt region refers to the central 11ML of Pt and the interface region refers to the Co and topmost 2ML of Pt (see right side in Fig. 4). We found from Fig. 4(a) that the SOC of the inside Pt region dominantly contributes to the σ_{xy}^S, whereas that of the interface region less affects over the entire energy range. This fact may be reflected by the trend described in Figs. 2 and 3(f) where the σ_{xy}^S increases when the number of Pt atomic layers increases.

We calculated spin Berry curvature as a function of $\mathbf{k}$, $\Omega_{xy}^S(\mathbf{k})$, for the Co/Pt$_{15}$ and mapped onto the 2D BZ in Figs. 5(a) and 5(b). At 0.1 eV, giving the maximum σ_{xy}^S in Fig. 3(f), the large positive contribution to $\Omega_{xy}^S(\mathbf{k})$ appears near $\overline{\mathrm{M}}'$ ($\overline{\mathrm{M}}$) and $\overline{\Gamma}$ points, where a sixfold rotational symmetry distribution of $\Omega_{xy}^S(\mathbf{k})$ is confirmed [see red region in Fig. 5(a)]. At −4.0 eV that shows the minimum σ_{xy}^S, the large negative $\Omega_{xy}^S(\mathbf{k})$ is seen in a $\overline{\Gamma}$-centered ring [see blue region in Fig. 5(b)]. To identify an origin, the band structure attributed to the inside Pt region in the Co/Pt$_{15}$ along high-symmetry line in the 2D BZ and the corresponding $\Omega_{xy}^S(\mathbf{k})$ contribution are plotted in Figs. 5(c)–5(e). In Fig. 5(e), there are widely dispersive $5d$ bands in an energy range from −6 to 1 eV. The dispersive bands crossing the Fermi level near $\overline{\mathrm{M}}'$ ($\overline{\mathrm{M}}$) point induce the large positive $\Omega_{xy}^S(\mathbf{k})$ [see magenta arrows in Figs. 5(c) and 5(e)]. These bands are focused in Fig. 5(f) for the cases with and without the SOC. When the SOC is not included, the $5d$ bands of the inside Pt are crossing just below the Fermi level in $\overline{\mathrm{M}}'$–$\overline{\Gamma}$ path [see dashed (yellow) line in left panel of Fig. 5(f)], but they are split out by the SOC [right panel of Fig. 5(f)], yielding a large positive contribution of $\Omega_{xy}^S(\mathbf{k})$ through a small value of denominator in Eq. (2). We

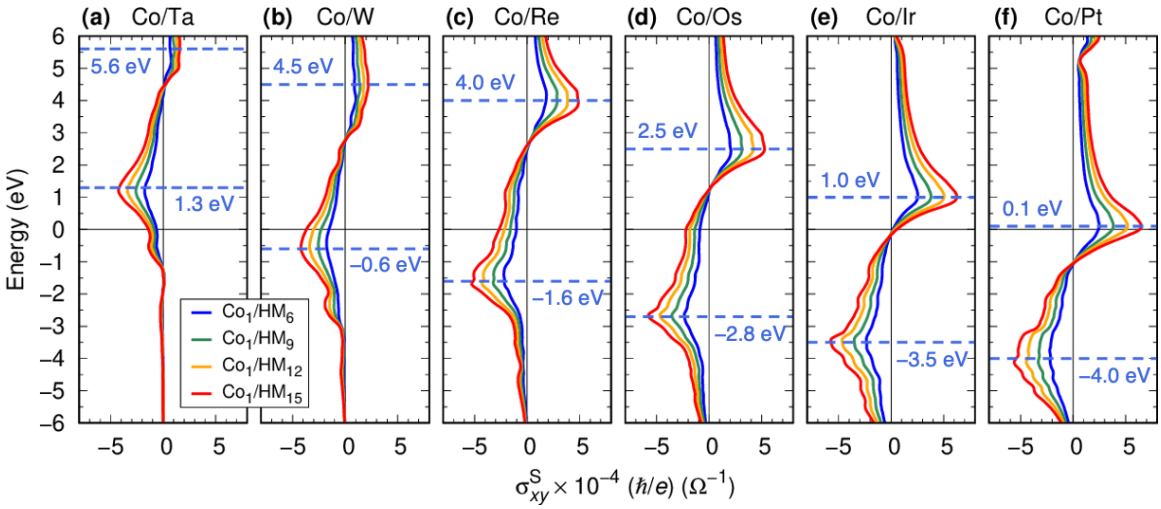

FIG. 3. Band-filling dependence of σ^{S}_{xy} for (a) Co/Ta$_n$, (b) Co/W$_n$, (c) Co/Re$_n$, (d) Co/Os$_n$, (e) Co/Ir$_n$, and (f) Co/Pt$_n$, where $n = 6$ (blue), 9 (green), 12 (orange), and 15 (red). Horizontal dashed lines (skyblue) indicate the energy levels that show the peaks of σ^{S}_{xy}, where the maximum and minimum values of Ω^{S}_{xy} appear in the higher and lower energy levels in all the systems. The Fermi level is set to zero.

note the fact that the $\overline{\mathrm{M}}$ ($\overline{\mathrm{M}}'$) point in the 2D BZ of the present system corresponds to X in the 3D BZ of fcc Pt in bulk, as shown in Fig. 1(d), at which the SOC-induced band splitting provides significant contribution to the spin Berry curvature [30]. It can be, therefore, concluded that the large σ^{S}_{xy} in the Co/Pt is attributed to the same origin in the bulk Pt. In the same way, at −4.0 eV, the SOC opens the energy gap near $\overline{\Gamma}$ point [Fig. 5(g)], and these bands induce the negative $\Omega^{S}_{xy}(\mathbf{k})$ [see purple arrows in Figs. 5(d) and 5(e)].

Figure 6 summarizes the 2D maps of $\Omega^{S}_{xy}(\mathbf{k})$ for the Co/HM$_{15}$ (HM = Ta, W, Re, Os, and Ir) at the energies that have the maximum and minimum values of σ^{S}_{xy} and the band structures, where sizes of symbols are weighted by the 5*d* states of inside HM regions. The $\Omega^{S}_{xy}(\mathbf{k})$ in the Co/bcc-HM systems shows a twofold rotation symmetry [Figs. 6(a) and 6(b)], whereas that in the Co/fcc-HM systems is in a sixfold rotation symmetry [Figs. 6(c)–6(e)]. This difference comes from the different stackings in the HM atomic layers, namely bcc and fcc stackings. Importantly, however, the $\mathbf{k}$ dependence of $\Omega^{S}_{xy}(\mathbf{k})$ is quite similar in each Co/bcc-HM and Co/fcc-HM system. In the Co/bcc-HM (HM = Ta, W), the positive and negative contributions of $\Omega^{S}_{xy}(\mathbf{k})$ at the energy levels of maximum and minimum σ^{S}_{xy} arise at near $\overline{\Gamma}$ in $\overline{\Gamma}$–$\overline{\mathrm{N}}$ line. Specifically, for the Co/W in Figs. 6(b) and 6(g), the bands of the inside W region along $\overline{\Gamma}$–$\overline{\mathrm{N}}$ at −0.6 eV give rise to the minimum σ^{S}_{xy} [$-4.21\times10^{-4}\,(\hbar/e)\,\Omega^{-1}$; $n = 15$]. These bands correspond to those of Γ–H line of the 3D BZ for bcc bulk W [see Fig. 1(c) for BZ] [41]. In the Co/fcc-HM (HM = Re, Os, Ir, Pt), the distribution of $\Omega^{S}_{xy}(\mathbf{k})$ are similar to the Co/Pt case [Figs. 6(c)–6(e)], although the energy levels of maximum and minimum σ^{S}_{xy}s are different [Figs. 6(h)–6(j)]. The band structure is essentially the same among the same stackings and the Fermi level only shifts due to the difference in the number of 5*d* electrons. Thus, the SHC in the Co/HM heterostructures is governed by the 5*d* band filling of band structure attributed to inside HM region, which is less affected by the Co film, meaning that a tuning of the Fermi level via hole or electron doping in the HM film can be a straightforward way to control the SHC. It notes that Zhang *et al.* clarify that the proximity-induced spin magnetic moment in the bulk HM reduces the SHC [74]. Even in the present system, the spin magnetic moment of HM in the interface region is proximity induced, which thus reduces the SHC as discussed in Fig. 4. However, the SHC in the whole heterostructure is dominated by the inside Pt region.

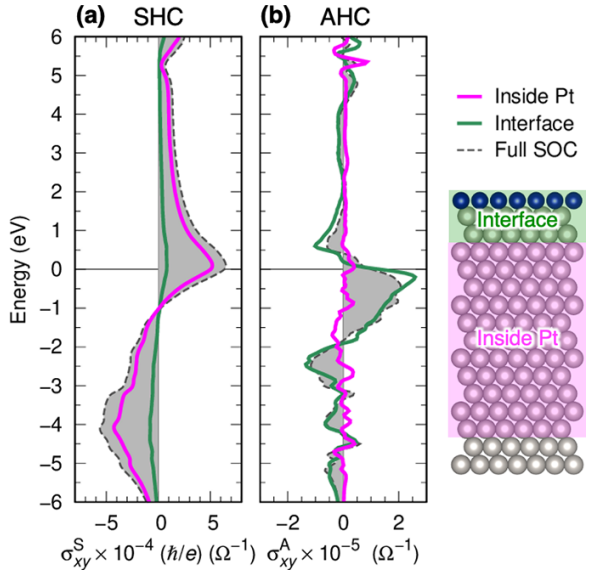

FIG. 4. Band-filling dependencies of (a) σ^{S}_{xy} and (b) σ^{A}_{xy} of Co/Pt$_{15}$, where SOC is turned on in either inside Pt region (magenta) or Co/Pt interfacial region (green). Results of full SOC calculations are shown in gray filled area. The Fermi level is set to zero.

B. Anomalous Hall conductivity

Figure 7 summarizes results of AHC (σ^{A}_{xy}). In contrast to the SHC, the value of σ^{A}_{xy} depends significantly only on the HM element but does not so on the HM thickness. The

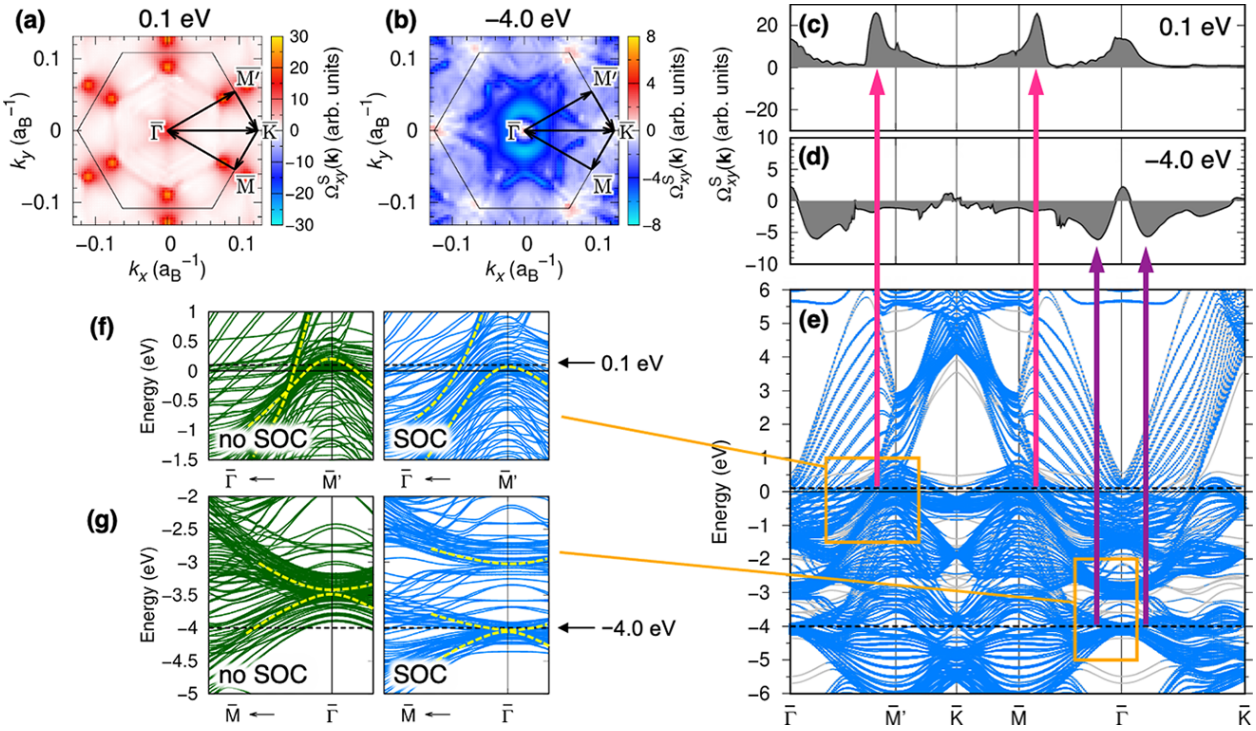

FIG. 5. Spin Berry curvature $\Omega^S_{xy}(\mathbf{k})$ mapped onto 2D BZ for Co/Pt_{15} at energy levels of (a) 0.1 eV and (b) −4.0 eV where the σ^S_{xy} shows the maximum and minimum values, respectively. Projection of $\Omega^S_{xy}(\mathbf{k})$ along high symmetry k path at (c) 0.1 eV and (d) −4.0 eV, and (e) band structure with size of symbol being weighted by contribution from 5d states inside the Pt region (defined by right side in Fig. 4). The k path is given in (a) and (b). (f) Band structures at around 0.1 eV near $\overline{M}'$ point without SOC (left) and with SOC (right), and (g) the same but at around −4.0 eV near Γ point. In (f) and (g), the dashed (yellow) lines are guides to eye (see main text for details). The Fermi level is set to zero.

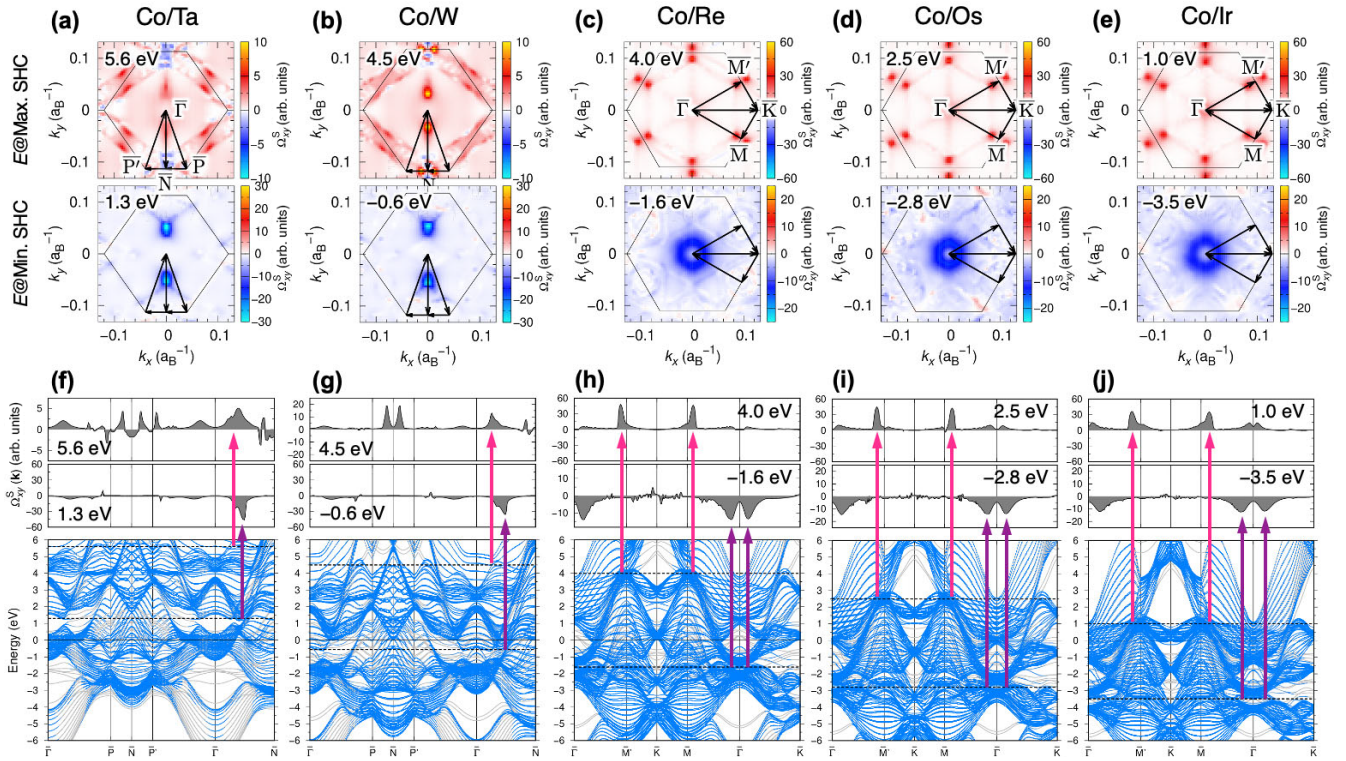

FIG. 6. [(a)–(e)] 2D BZ mapping of $\Omega^S_{xy}(\mathbf{k})$ for Co/HM_{15} (HM = Ta, W, Re, Os, Ir), energy of which shows the energy level with the maximum (top) and minimum (bottom) σ^S_{xy}s. [(f)–(j)] Projections of $\Omega^S_{xy}(\mathbf{k})$ (top and middle) and 5d band structures of inside HM regions (bottom). The Fermi level is set to zero.

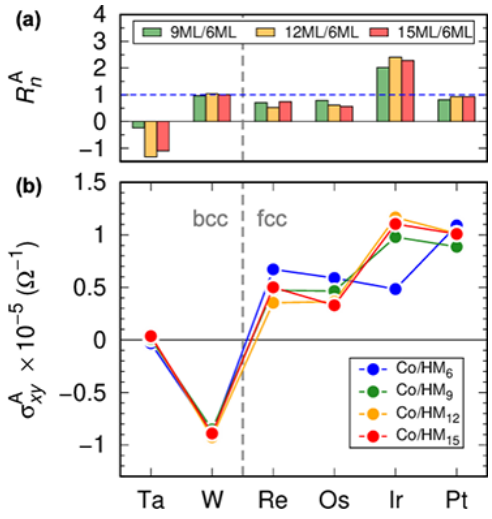

FIG. 7. (a) Change ratio of σ_{xy}^{A} against HM thickness, $R_n^A = \sigma_{xy,n}^A/\sigma_{xy,6}^A$, and (b) σ_{xy}^{A} for Co/HM$_n$ (HM = Ta, W, Re, Os, Ir, Pt). The notations are the same as in Fig. 2.

negative value of σ_{xy}^{A} is found in the Co/W$_n$, and all the others show the positive σ_{xy}^{A}s except Co/Ta$_n$, as shown in Fig. 7(b). For the HM thickness dependence, Fig. 7(a) shows the change ratio of σ_{xy}^{A} from Co/HM$_6$, $R_n^A = \sigma_{xy,n}^A/\sigma_{xy,6}^A$ where $\sigma_{xy,6}^A$ ($\sigma_{xy,n}^A$) is referred to as the value of σ_{xy}^{A} of Co/HM$_6$ (Co/HM$_n$; n = 9, 12, 15). The Co/W$_n$ and Co/Pt$_n$ systems show $R_n^A \sim 1$, indicating that σ_{xy}^{A} is independent of the HM thickness. In the Co/Re$_n$ and Co/Os$_n$ systems, the R_n^A remains a constant value less than 1. This means that the σ_{xy}^{A} for $n = 9$, 12, and 15 are almost constant and slightly higher than that in $n = 6$. On the other hand, the R_n^A of Co/Ir$_n$ shows large value more than 1 but no significant changes with respect to n. Therefore, it can be concluded that the σ_{xy}^{A} in Co/HM$_n$ does not show considerable HM-thickness dependence, although the value of σ_{xy}^{A} for $n = 6$ is eventually large (small) compared to those for $n = 9$, 12, and 15 in Co/Re$_n$ and Co/Os$_n$ (Co/Ir$_n$). Among these, the maximum of σ_{xy}^{A} is found in the Co/Pt$_n$ ($1.09\times10^{-5}\,\Omega^{-1}$) for thin HM atomic layers ($n = 6$) and in the Co/Ir$_n$ ($1.10\times10^{-5}\,\Omega^{-1}$) and Co/Pt$_n$ ($1.01\times10^{-5}\,\Omega^{-1}$) for thick HM atomic layers ($n = 15$). In the Co/W$_n$, the negatively large value of σ_{xy}^{A} is obtained; $-0.89\times10^{-5}\,\Omega^{-1}$ for $n = 15$. The σ_{xy}^{A} in the Co/Ta$_n$ is quite small in Fig. 7(b).

The band-filling dependencies of σ_{xy}^{A} are given in Fig. 8. The dependencies are rather complex compared to those in the SHC. There are no systematic trends among all the systems but exist local peaks of σ_{xy}^{A} in the range of $-3 \sim 2$ eV (see filled area in Fig. 8), which corresponds to the band width at the Co atomic layer. The peak heights hardly change as the HM thickness increases for all the systems. In the Co/Ta$_n$, the sign of σ_{xy}^{A} is changed at the zero energy and hence the σ_{xy}^{A} is small [Fig. 8(a)]. However, in the rest systems, the local peaks or shoulders of σ_{xy}^{A} are located near the zero energy [Figs. 8(b)–8(f)], resulting in the significant dependence against the HM element as described in Fig. 7(b).

Taking the Co/Pt$_{15}$ as an example, we discuss the effect of SOC to the AHC by the spatially-resolved analysis, as given in Fig. 4(b). We find that the effect of SOC at the interface region is more dominant compared to that of the inside Pt region, which is opposite to the SHC.

In Fig. 9(a), the distribution of the Berry curvature $\Omega_{xy}^{A}(\mathbf{k})$ at the zero energy shows almost mirror symmetry with a sign change with respect to the k_x (or k_y) axis, in which large values of positive and negative contributions appear at $\overline{\mathrm{M}}$ and $\overline{\mathrm{M}}'$ points, respectively. However, they do not cancel out when integrated in the 2D BZ, leaving a nonzero (positive) value, $\sigma_{xy}^{A} = 1.01\times10^{-5}\,\Omega^{-1}$. This fact is confirmed in the bottom of Fig. 9(b) where the shape and height of the peaks are slightly different between $\overline{\mathrm{M}}$ and $\overline{\mathrm{M}}'$ points (see circles in the figure). To see more clearly, asymmetric component with

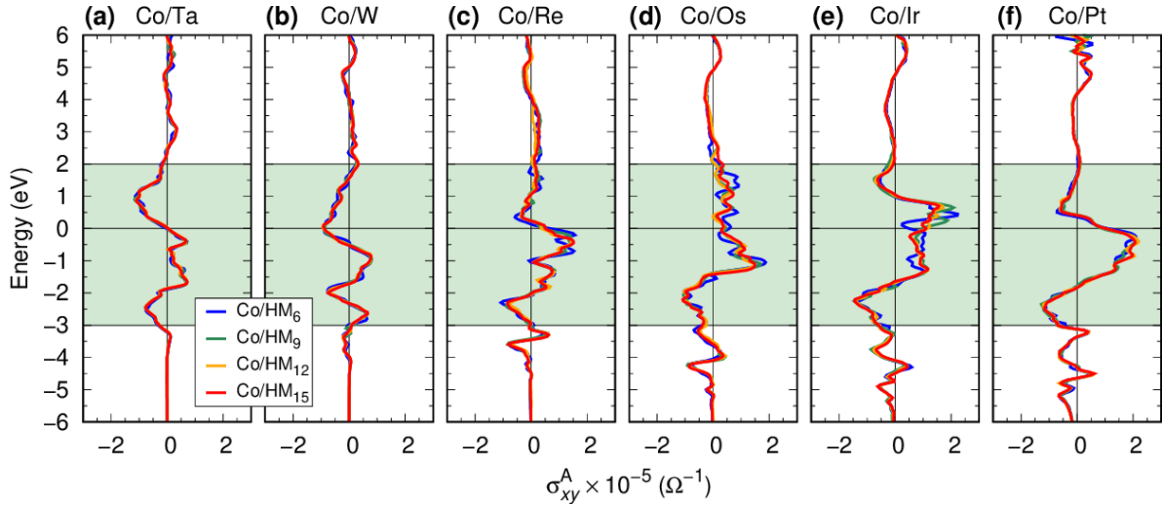

FIG. 8. Band-filling dependence of σ_{xy}^{A} for (a) Co/Ta$_n$, (b) Co/W$_n$, (c) Co/Re$_n$, (d) Co/Os$_n$, (e) Co/Ir$_n$, and (f) Co/Pt$_n$, where $n = 6$ (blue), 9 (green), 12 (orange), and 15 (red). Green-filled area from -3 to 2 eV is the energy range where local peaks of σ_{xy}^{A} appear. The Fermi level is set to zero.

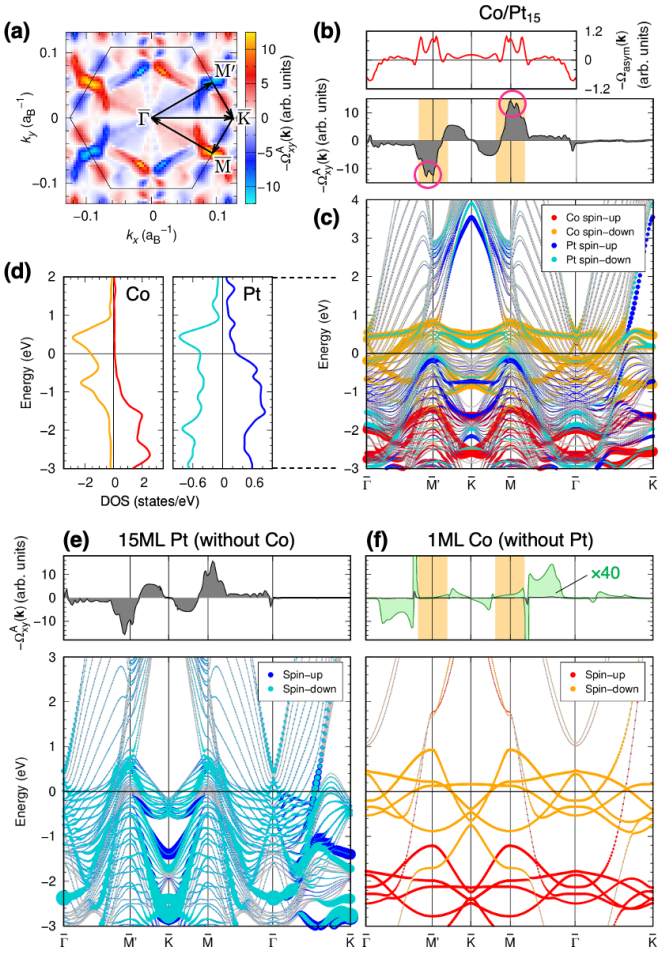

FIG. 9. (a) 2D-BZ mapping of $\Omega^{A}_{xy}(\mathbf{k})$, (b) projection of $\Omega^{A}_{xy}(\mathbf{k})$ of high-symmetry k path (bottom) and asymmetric component of $\Omega^{A}_{xy}(\mathbf{k})$ with respect to K point $\Omega_{asym}(\mathbf{k})$ (top; see text for more details), and (c) band structure for Co/Pt_{15}. Sizes of symbols in the band structure are weighted by contributions from Co-3d states (red and orange colors show spin-up and -down states) and interfacial Pt-5d states (blue and skyblue colors show spin-up and -down states). (d) DOS for Co 3d (left) and Pt 5d (right) states. (e) $\Omega^{A}_{xy}(\mathbf{k})$ and band structure for non-spin-polarized 15ML Pt (without Co), and (f) those for spin-polarized Co monolayer (without Pt). In top panel of (f), green-filled area shows the results multiplied by 40. The Fermi level is set to zero.

respect to the K point is extracted from $\Omega^{A}_{xy}(\mathbf{k})$ as $\Omega_{asym}(\mathbf{k}) = \Omega^{A}_{xy}(\mathbf{k}) - \Omega_{sym}(\mathbf{k})$, where $\Omega_{sym}(\mathbf{k})$ is the component of symmetric distribution, $\frac{1}{2}[\Omega^{A}_{xy}(\mathbf{k}) - \Omega^{A}_{xy}(-\mathbf{k})]$, with respect to the K point; i.e., $\mathbf{k} = (k_x, k_y)$ and $-\mathbf{k} = (k_x, -k_y)$, and plotted in top of Fig. 9(b). The $\Omega_{asym}(\mathbf{k})$ shows positive peaks at around $\overline{M}$ and $\overline{M'}$ points, indicating that the absolute value of $\Omega^{A}_{xy}(\mathbf{k})$ at $\overline{M}$ point is greater than that at $\overline{M'}$ point in the bottom of Fig. 9(b). Figure 9(c) presents the band structure in which the exchange splitting of Pt-5d bands around the Fermi level is introduced due to the orbital hybridization with the interfacial Co, which is more visible from density of states (DOS) in Fig. 9(d). To obtain an insight into roles of interfacial Co and Pt, we calculated $\Omega^{A}_{xy}(\mathbf{k})$s for slabs consisting of 15ML Pt and free-standing 1ML Co, separately, and the results are

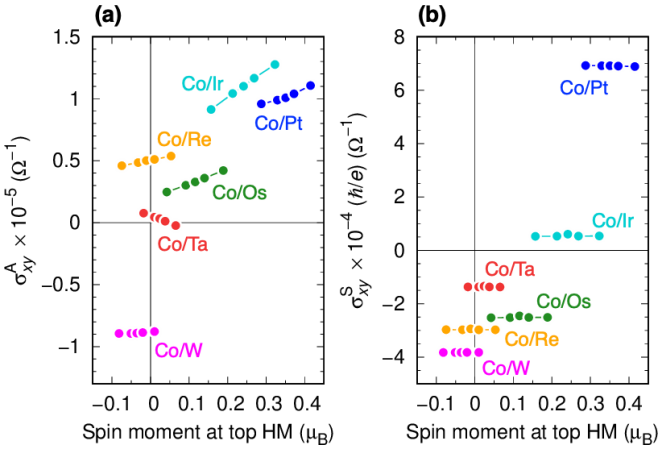

FIG. 10. Variations of (a) σ^{A}_{xy} and (b) σ^{S}_{xy} as a function of spin magnetic moment at the interfacial HM atomic layer for the Co/HM_{15}, where different colors indicate HM = Ta (red), W (magenta), Re (orange), Os (green), Ir (skyblue), and Pt (blue), respectively.

given in Figs. 9(e) and 9(f). Since the Pt is nonmagnetic and the bands are not spin polarized even at the surface Pt atomic layer, the distributions of $\Omega^{A}_{xy}(\mathbf{k})$ along $\overline{\Gamma}$–$\overline{M'}$–$\overline{K}$ and $\overline{\Gamma}$–$\overline{M}$–$\overline{K}$ paths are perfectly mirror symmetric with the sign change with respect to the K point [see Fig. 9(e)]. The resultant AHC is explicitly zero. On the other hand, in the 1ML Co, the breaking of the time-reversal symmetry gives an asymmetric distribution in $\Omega^{A}_{xy}(\mathbf{k})$ [see green plot especially at around $\overline{M'}$ and $\overline{M}$ points in top of Fig. 9(f)], leading that the σ^{A}_{xy} is $3.35\times10^{-5}\ \Omega^{-1}$. It is further emphasized that the scale of $\Omega^{A}_{xy}(\mathbf{k})$ in the nonmagnetic 15ML Pt is the same order in Co/Pt_{15} system but several ten times greater than that in the ferromagnetic 1ML Co. These facts conclude that magnitude of the AHC is affected by the Berry curvature at the interfacial Pt atomic layer, while the ferromagnetism at Co plays a role to induced the exchange splitting in bands of the interfacial Pt through the proximity effect. To evident this, we performed calculations for the Co/Pt where the spin magnetic moment at the interfacial Pt atomic layer is artificially introduced. As shown in Fig. 10(a), the σ^{A}_{xy} for the Co/Pt is proportionally varied against the scale of introduced spin magnetic moment.

In the case of other Co/HM_{15} systems (HM = Ta, W, Re, Os, Ir), the induced spin magnetic moment at the interfacial HM atomic layer by the proximity effect brings nonzero AHC value. In Figs. 11(a)–11(e), the $\Omega^{A}_{xy}(\mathbf{k})$ depends on the HM element, where the almost mirror symmetric distributions can be seen in the 2D BZs for all the systems, while the $\mathbf{k}$ integrations of the $\Omega^{A}_{xy}(\mathbf{k})$s over the BZ result in the nonzero values of σ^{A}_{xy}. In bottom two figures of Figs. 11(f)–11(j), the weights of the 3d and 5d orbitals in the band structures indicate that the Co 3d bands strongly hybridize with the HM 5d bands. The energy level of this hybridized bands moves to lower energy as the number of 5d electrons increases. It is thus found that the occupied 5d bands near the Fermi level (zero energy) determine the overall distribution of $\Omega^{A}_{xy}(\mathbf{k})$; in second figures from the top of Figs. 11(f)–11(j), scale and

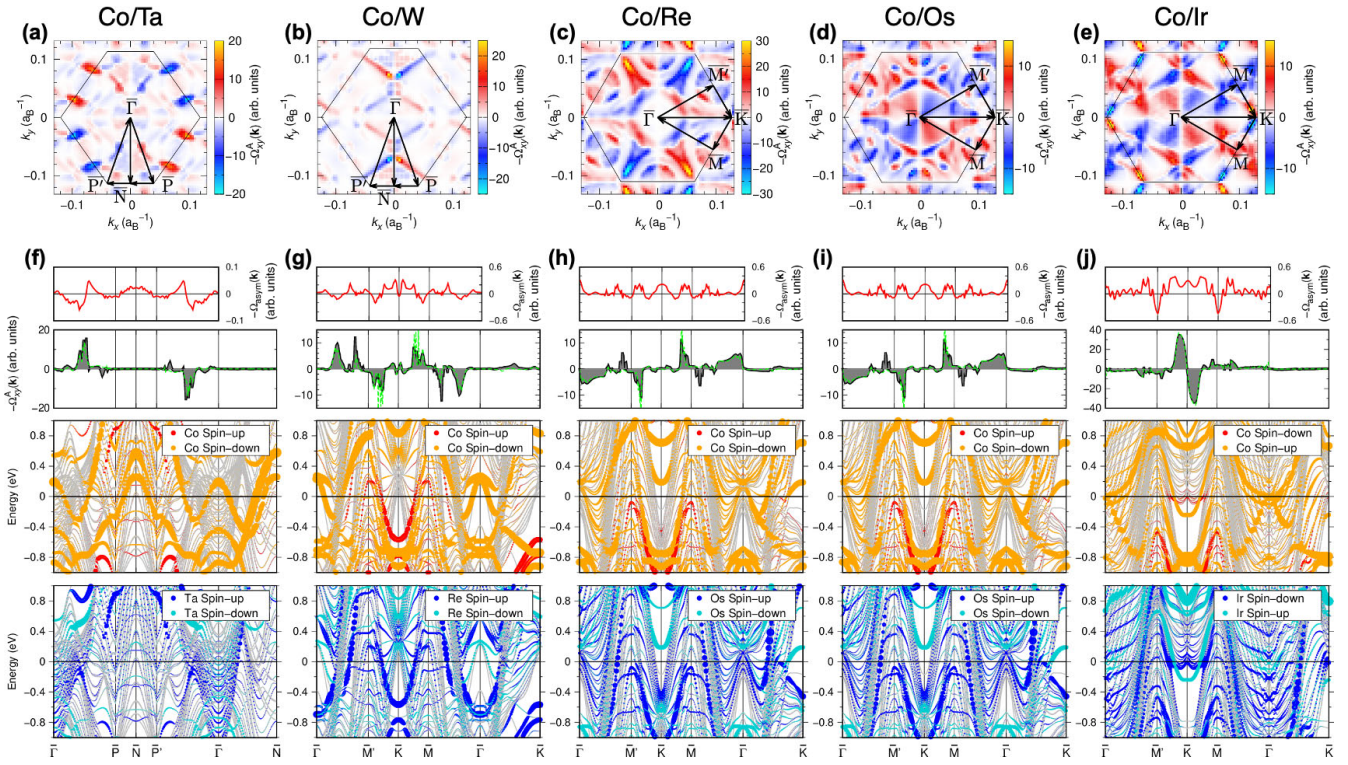

FIG. 11. [(a)–(e)] 2D-BZ mapping of $\Omega^{\mathrm{A}}_{xy}(\mathbf{k})$ for Co/HM_{15} (HM = Ta, W, Re, Os, Ir) at Fermi level. [(f)–(j)] $\Omega^{\mathrm{A}}_{xy}(\mathbf{k})$ [second from top; green-dashed lines are $\Omega^{\mathrm{A}}_{xy}(\mathbf{k})$ calculated from non-spin-polarized 15ML HM (without Co) for references], its asymmetric component, $\Omega_{\mathrm{asym}}(\mathbf{k})$ (top), and band structures of interfacial Co 3*d* and HM 5*d* (bottom two). Sizes of symbols in band structure are weighted by contributions from Co 3*d* states (red and orange colors show spin-up and -down states) and HM 5*d* states (blue and skyblue colors show spin-up and -down states). The Fermi level is set to zero.

shape of the $\Omega^{\mathrm{A}}_{xy}(\mathbf{k})$ in Co/HM_{15} (gray filled area) follow those in 15ML HM system without Co (green-dashed line). Specifically, in Co/Ir that shows the largest σ^{A}_{xy}, there exist flat Ir 5*d* bands hybridizing with Co 3*d* bands at the Fermi level near $\overline{\mathrm{K}}$ point [bottom two plots in Fig. 11(j)]. The existence of the interfacial hybridized bands allows the asymmetric distribution of $\Omega^{\mathrm{A}}_{xy}(\mathbf{k})$ along $\overline{\mathrm{K}}$–$\overline{\mathrm{M}}'$ and $\overline{\mathrm{K}}$–$\overline{\mathrm{M}}$ paths, resulting in the positive Ω^{A}_{xy} ($1.10\times10^{-5}\,\Omega^{-1}$), as confirmed in top two plots in Fig. 11(j). Similar tendency is confirmed in other systems [Figs. 11(f)–11(i)]. For the Co/Ta, since the most Ta-5*d* bands hybridizing with Co 3*d* locate above 0.4 eV and only a few bands remain on the Fermi level, the asymmetry in $\Omega^{\mathrm{A}}_{xy}(\mathbf{k})$ becomes rather weak, so that the resultant Ω^{A}_{xy} is negligibly small.

Moreover, the interfacial hybridization between the Co and HM modulates the value of σ^{A}_{xy} by the induced spin magnetic moment of the HM atomic layer at the interface. As shown in Fig. 10(a), when the spin magnetic moment is artificially introduced at the interfacial HM atomic layer, the σ^{A}_{xy} is proportional to the magnitude of spin magnetic moment. Although the modulation of AHC by the introduced spin magnetic moment is confirmed, clearly this effect is not significant compared to the HM element dependence. Note that, in Co/W and Co/Re systems, even when the sign of spin magnetic moment of HM changes, the σ^{A}_{xy} keeps same sign. This is because the spin of Co remains same sign ($1.58 \sim 1.59\,\mu_{\mathrm{B}}$ for Co in Co/W_{15} and Co/Re_{15}) with tiny changes ($\sim$0.01 μ_{B}) by rehybridization with the top HM, which is one order of magnitude smaller than that of HM. It notes that since the sign change of σ^{A}_{xy} in Co/Ta occurs around the Fermi level in Fig. 8(a), the σ^{A}_{xy} in Fig. 10(a) is sensitive to the introduced spin magnetic moment of top HM, although σ^{A}_{xy} is small value. For the SHC, however, no dependence against the introduced spin magnetic moment is confirmed [Fig. 10(b)], as the SHC is governed by the band structure of the inside HM. It may further note that the chemical trend of σ^{A}_{xy} to the HM elements even for thick Co films follows that in Fig. 7, since the spin magnetic moment of the interfacial Co is almost constant regardless of the Co thickness [75], although the absolute value may be governed by the thick Co films.

It is experimentally reported that the interfacial SOC of FM/HM interface, namely ISOC, which can be characterized by AHC or PMA, is desired to be small for efficient magnetization switching of adjacent FM layers [76]. Note that the flow of spin current is in-plane direction in our calculations and this may be different from device architectures where the spin current is injected from HM layer to FM layer. Therefore, the direct comparison is not allowed. However, in the context of optimizing the ISOC, our results can be a guideline for appropriate material choice of HM element. The present study invites further experimental and theoretical investigations on the AHC in 3*d* FM/5*d* HM heterostructures.

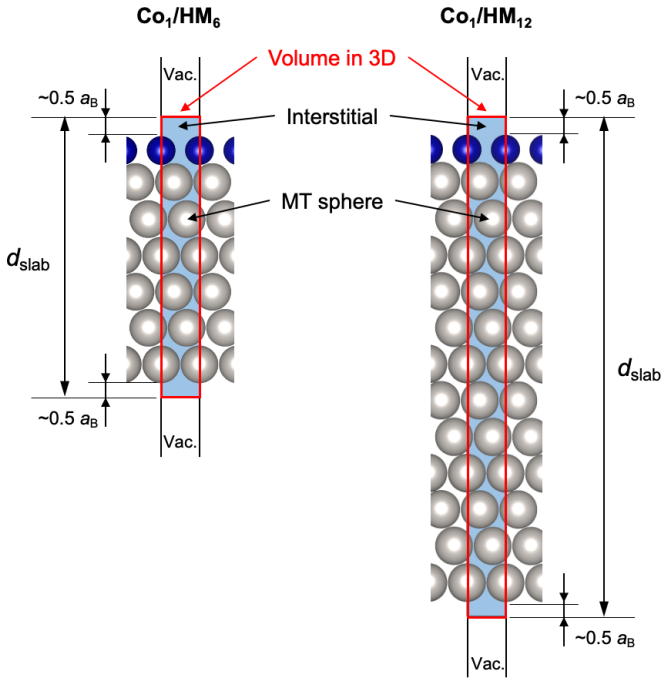

FIG. 12. Geometries of 2D slab structures consisting of MT spheres, interstitial, and semi-infinite vacuum (Vac.) regions: For example, Co/HM$_n$ systems with $n = 6$ (left) and 12 (right) in fcc stacking of HM are shown. Solid (red) square defines the volume in 3D system, where z length corresponds to $d_{\rm slab}$. See main text for more details.

IV. SUMMARY

The SHC and AHC in the Co/5d HM (Ta, W, Re, Os, Ir, and Pt) are investigated by the first-principles calculations, and the roles of Co and HM were elucidated. For the SHC, positive and negative maximum values are obtained in the Co/Pt$_{15}$ [6.35×10^{-4} $(\hbar/e)\,\Omega^{-1}$) and Co/W$_{15}$ [-3.69×10^{-4} $(\hbar/e)\,\Omega^{-1}$], in which the scale and sign of $\sigma^{\rm S}_{xy}$ systematically depend on the chemical (HM element) trend due to the different number of 5d electrons. This SHC is caused by the spin Berry curvature in 5d bands inside the HM atomic layers, thus, a doping of electron/hole into the HM layers can be an effective approach to modulate these bands for controlling the SHC. For the AHC, the positive maximum $\sigma^{\rm A}_{xy}$ is obtained in the Co/Ir$_{15}$ ($1.10\times10^{-5}\,\Omega^{-1}$) and Co/Pt$_{15}$ ($1.01\times10^{-5}\,\Omega^{-1}$) and negative maximum is in the Co/W$_{15}$ ($-0.89\times10^{-5}\,\Omega^{-1}$). The AHC depends only on the HM element but does not so on the HM thickness. The origin is interpreted by the Berry curvature of the 5d bands hybridizing with the Co 3d bands near the Fermi level and by the proximity effect of Co playing a role to induce the spin magnetic moment into the HM at the interface. Our anatomy provides guidelines to design Co/HM heterostructures where an appropriate choice of HM element, Fermi-level tuning, and interfacial modification can be effective to control the SHC and AHC for suitable performance of spin-orbitronics applications.

ACKNOWLEDGMENTS

Authors thank Y. Nagato for fruitful discussion. This work is partly supported by KAKENHI (Grants No. JP23H00176, No. JP22K14290, No. JP21K03444, No. JP21H04562, and No. JP19K03716); the Okasan-Kato Foundation; the Research Foundation for the Electrotechnology of Chubu; the Tatematsu Foundation; Cooperative Research Project of the Research Institute of Electrical Communication, Tohoku University; the Data-Science Research Center for Material, Quantum, and Measurement Technologies, Mie University; and the Center for Spintronics Research Network, Osaka University. Numerical calculations were partially performed using computational facilities at Research Institute for Information Technology, Kyushu University and the Numerical Materials Simulator at NIMS.

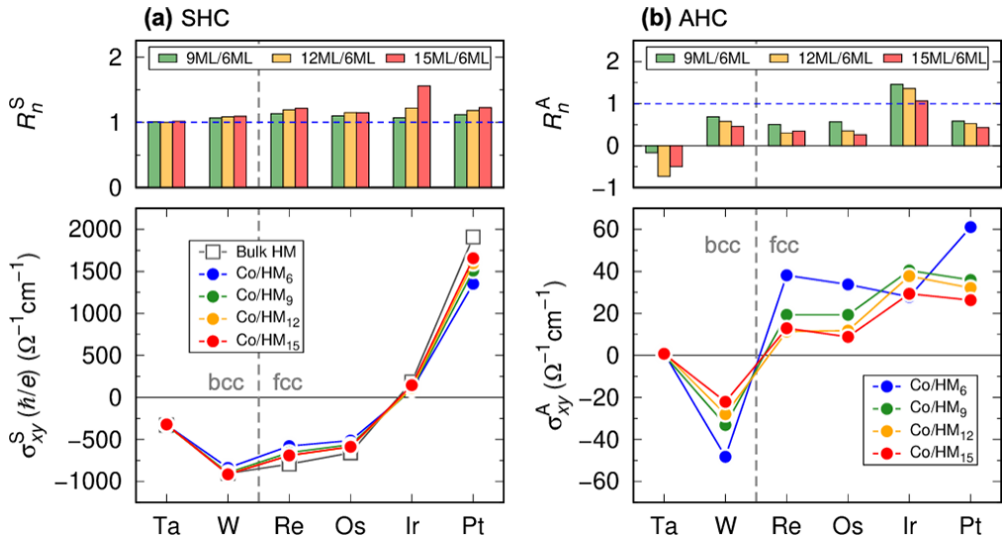

FIG. 13. Calculated (a) $\Omega^{\rm S}_{xy}$ and (b) $\Omega^{\rm A}_{xy}$, which are the same results as those in Figs. 2 and 7 but in volume in 3D unit (Ω^{-1}cm^{-1}). In bottom panel of (a), results in bulk HM are shown as a reference (opened squares). The notations are the same as those in Figs. 2 and 7.

APPENDIX: SPIN HALL AND ANOMALOUS HALL CONDUCTIVITIES IN VOLUME IN 3D UNIT

In the present calculations [64–66], the model is constructed by a single slab region (MT spheres and interstitial) and two semi-infinite vacuum regions at the top and bottom sides of the slab, as shown in Fig. 12. We set the height of the slab ($d_{\rm slab}$) to be a distance of about 0.5 $a_{\rm B}$ away from the outermost MT spheres regardless of the HM element and its thickness (n). To convert the unit of SHC and AHC into the 3D unit, the $\sigma^{\rm S}_{xy}$ and $\sigma^{\rm A}_{xy}$ in the present calculations (in 2D unit) are divided by the $d_{\rm slab}$, where the V is given by $A\times d_{\rm slab}$.

The results in the 3D unit ($\Omega^{-1}{\rm cm}^{-1}$) are presented in Fig. 13. For the SHC, in Fig. 13(a), the $\sigma^{\rm S}_{xy}$ increases and approaches the bulk values as increasing the HM thickness; it is clear especially in the Co/Pt$_n$ system (see bottom figure). The overall characteristics of the SHC in the 3D unit follow the results of the 2D unit in Fig. 2, in which, however, quantitative values of the $R^{\rm S}_n$ tend to differ between 2D and 3D units because of the $d_{\rm slab}$ depending on the HM element and its thickness in the system. The sign change between Co/Os$_n$ and Co/Ir$_n$ heterostructures remains a discrepancy from the bulk HM calculations [31] where the sign changes between Re and Os. This can be caused by the different crystal structures of Re and Os, for which the fcc structure is assumed in the present work while the hcp structure in the earlier calculations [31].

In Fig. 13(b), the AHC shows the HM-thickness dependence where the $\sigma^{\rm A}_{xy}$ decreases as increasing the HM thickness. Since the AHC originates from the interfacial band structures as discussed in Sec. III B, the absolute value of $\sigma^{\rm A}_{xy}$ becomes apparently small by dividing by the volume of unit cell ($V = A\times d_{\rm slab}$) instead of unit area of unit cell (A) in Eq. (1). This results in that the $R^{\rm A}_n$ appears to depend on the HM thickness, which is not the case for the results in 2D unit.

[1] S. Rüegg, G. Schütz, and R. Wienke, Spin-dependent x-ray absorption in Co/Pt multilayers, J. Appl. Phys. **69**, 5655 (1991).

[2] G. Schütz, S. Stähler, M. Knülle, and P. Fischer, Distribution of magnetic moments in Co/Pt and Co/Pt/Ir/Pt multilayers detected by magnetic x-ray absorption, J. Appl. Phys. **73**, 6430 (1993).

[3] M. Suzuki, H. Muraoka, Y. Inaba, H. Miyagawa, N. Kawamura, T. Shimatsu, H. Maruyama, N. Ishimatsu, Y. Isohama, and Y. Sonobe, Depth profile of spin and orbital magnetic moments in a subnanometer Pt film on Co, Phys. Rev. B **72**, 054430 (2005).

[4] K. Nakamura, R. Shimabukuro, Y. Fujiwara, T. Akiyama, T. Ito, and A. J. Freeman, Giant modification of the magnetocrystalline anisotropy in transition-metal monolayers by an external electric field, Phys. Rev. Lett. **102**, 187201 (2009).

[5] S. Ikeda, K. Miura, H. Yamamoto, K. Mizunuma, H. D. Gan, M. Endo, S. Kanai, J. Hayakwawa, F. Matsukura, and H. Ohno, A perpendicular-anisotropy CoFeB-MgO magnetic tunnel junction, Nat. Mater. **9**, 721 (2010).

[6] D. Chiba, M. Kawaguchi, S. Fukami, N. Ishiwata, K. Shimamura, K. Kobayashi, and T. Ono, Electric-field control of magnetic domain-wall velocity in ultrathin cobalt with perpendicular magnetization, Nat. Commun. **3**, 888 (2012).

[7] B. Dieny and M. Chshiev, Perpendicular magnetic anisotropy at transition metal/oxide interfaces and applications, Rev. Mod. Phys. **89**, 025008 (2017).

[8] A.-M. Pradipto, K. Yakushiji, W. S. Ham, S. Kim, Y. Shiota, T. Moriyama, K.-W. Kim, H.-W. Lee, K. Nakamura, K. J. Lee, and T. Ono, Enhanced perpendicular magnetocrystalline anisotropy energy in an artificial magnetic material with bulk spin-momentum coupling, Phys. Rev. B **99**, 180410(R) (2019).

[9] A. Fert, V. Cros, and J. Sampaio, Skyrmions on the track, Nat. Nanotech. **8**, 152 (2013).

[10] K. Yamamoto, A.-M. Pradipto, K. Nawa, T. Akiyama, T. Ito, T. Ono, and K. Nakamura, Interfacial Dzyaloshinskii-Moriya interaction and orbital magnetic moments of metallic multilayer films, AIP Adv. **7**, 056302 (2017).

[11] I. Mihai Miron, G. Gaudin, S. Auffret, B. Rodmacq, A. Schuhl, S. Pizzini, J. Vogel, and P. Gambardella, Current-driven spin torque induced by the Rashba effect in a ferromagnetic metal layer, Nat. Mater. **9**, 230 (2010).

[12] L. Liu, C.-F. Pai, Y. Li, H. W. Tseng, D. C. Ralph, and R. A. Buhrman, Spin-torque switching with the giant spin Hall effect of tantalum, Science **336**, 555 (2012).

[13] H. Nakayama, M. Althammer, Y.-T. Chen, K. Uchida, Y. Kajiwara, D. Kikuchi, T. Ohtani, S. Geprägs, M. Opel, S. Takahashi, R. Gross, G. E. W. Bauer, S. T. B. Goennenwein, and E. Saitoh, Spin Hall magnetoresistance induced by a nonequilibrium proximity effect, Phys. Rev. Lett. **110**, 206601 (2013).

[14] F. Hellman, A. Hoffmann, Y. Tserkovnyak, G. S. D. Beach, E. E. Fullerton, C. Leighton, A. H. MacDonald, D. C. Ralph, D. A. Arena, H. A. Durr *et al.*, Interface-induced phenomena in magnetism, Rev. Mod. Phys. **89**, 025006 (2017), and references therein.

[15] S. Bhatti, R. Sbiaa, A. Hirohata, H. Ohno, S. Fukami, and S. N. Piramanayagam, Spintronics based random access memory: A review, Mater. Today **20**, 530 (2017).

[16] B. Dieny, R. B. Goldforb, and K. J. Lee, *Introduction to Magnetic Random-Access Memory* (Wiley, New York, 2016).

[17] M. I. Dyakonov and V. Perel, Current-induced spin orientation of electrons in semiconductor, Phys. Lett. A **35**, 459 (1971).

[18] J. E. Hirsch, Spin Hall effect, Phys. Rev. Lett. **83**, 1834 (1999).

[19] S. Zhang, Spin Hall effect in the presence of spin diffusion Phys. Rev. Lett. **85**, 393 (2000).

[20] J. Sinova, S. O. Valenzuela, J. Wunderlich, C. H. Back, and T. Jungwirth, Spin Hall effects, Rev. Mod. Phys. **87**, 1213 (2015), and references therein.

[21] R. Karplus and J. M. Luttinger, Hall effect in ferromagnetics, Phys. Rev. **95**, 1154 (1954).

[22] J. Smit, The spontaneous Hall effect in ferromagnetics I, Physica **21**, 877 (1955).

[23] N. Nagaosa, J. Sinova, S. Onoda, A. H. MacDonald, and N. P. Ong, Anomalous Hall effect, Rev. Mod. Phys. **82**, 1539 (2010), and references therein.

[24] S. A. Wolf, D. D. Awschalom, R. A. Buhrman, J. M. Daughton, S. V. Molnár, M. L. Roukes, A. Y. Chtchelkanova, and D. M.

Treger, Spintronics: A spin-based electronics vision for the future, Science **294**, 1488 (2001).
[25] C. Chappert, A. Fert, and F. N. V. Dau, The emergence of spin electronics in data storage, Nat. Mater. **6**, 813 (2007).
[26] D. Chiba, M. Yamanouchi, F. Matsukura, and H. Ohno, Electrical manipulation of magnetization reversal in a ferromagnetic semiconductor, Science **301**, 943 (2003).
[27] G. Yang, G. Li, X. Chen, J. Zhang, and G. Yu, Ultrasensitive anomalous Hall effect in Ta/CoFe/oxide/Ta multilayers, Adv. Condens. Matter Phys. **2016**, 9734610 (2016).
[28] T. Zhu, P. Chen, Q. H. Zhang, R. C. Yu, and B. G. Liu, Giant linear anomalous Hall effect in the perpendicular CoFeB thin films, Appl. Phys. Lett. **104**, 202404 (2014).
[29] Y. M. Lu, J. W. Cai, H. Y. Pan, and L. Sun, Ultrasensitive anomalous Hall effect in SiO_2/Fe-Pt/SiO_2 sandwich structure films, Appl. Phys. Lett. **100**, 022404 (2012).
[30] G. Y. Guo, S. Murakami, T.-W. Chen, and N. Nagaosa, Intrinsic spin Hall effect in platinum: First-principles calculations, Phys. Rev. Lett. **100**, 096401 (2008).
[31] T. Tanaka, H. Kontani, M. Naito, T. Naito, D. S. Hirashima, K. Yamada, and J. Inoue, Intrinsic spin Hall effect and orbital Hall effect in 4*d* and 5*d* transition metals, Phys. Rev. B **77**, 165117 (2008).
[32] E. Sagasta, Y. Omori, S. Vélez, R. Llopis, C. Tollan, A. Chuvilin, L. E. Hueso, M. Gradhand, Y. C. Otani, and F. Casanova, Unveiling the mechanisms of the spin Hall effect in Ta, Phys. Rev. B **98**, 060410(R) (2018).
[33] F. Freimuth, S. Blügel, and Y. Mokrousov, Anisotropic spin Hall effect from first principles, Phys. Rev. Lett. **105**, 246602 (2010).
[34] M. Morota, Y. Niimi, K. Ohnishi, D. H. Wei, T. Tanaka, H. Kontani, T. Kimura, and Y. Otani, Indication of intrinsic spin Hall effect in 4*d* and 5*d* transition metals, Phys. Rev. B **83**, 174405 (2011).
[35] Y. Yao, L. Kleinman, A. H. MacDonald, J. Sinova, T. Jungwirth, D.-S. Wang, E. Wang, and Q. Niu, First principles calculation of anomalous Hall conductivity in ferromagnetic bcc Fe, Phys. Rev. Lett. **92**, 037204 (2004).
[36] X. Wang, J. R. Yates, I. Souza, and D. Vanderbilt, *Ab initio* calculation of the anomalous Hall conductivity by Wannier interpolation, Phys. Rev. B **74**, 195118 (2006).
[37] X. Wang, D. Vanderbilt, J. R. Yates, and I. Souza, Fermi-surface calculation of the anomalous Hall conductivity, Phys. Rev. B **76**, 195109 (2007).
[38] H.-R. Fuh and G.-Y. Guo, Intrinsic anomalous Hall effect in nickel: A GGA + U study, Phys. Rev. B **84**, 144427 (2011).
[39] A. Asamitsu, T. Miyasato, N. Abe, T. Fujii, Y. Onose, S. Onoda, N. Nagaosa, and Y. Tokura, Anomalous Hall effect and nernst effect in itinerant ferromagnets, J. Magn. Magn. Mater. **310**, 2000 (2007).
[40] L. Ye, Y. Tian, X. Jin, and D. Xiao, Temperature dependence of the intrinsic anomalous Hall effect in nickel, Phys. Rev. B **85**, 220403(R) (2012).
[41] X. Sui, C. Wang, J. Kim, J. Wang, S. H. Rhim, W. Duan, and N. Kioussis, Giant enhancement of the intrinsic spin Hall conductivity in β-tungsten via substitutional doping, Phys. Rev. B **96**, 241105(R) (2017).
[42] L. Qian, K. Wang, Y. Zheng, and G. Xiao, Spin Hall effect in the α and β phases of Ta_xW_{1-x} alloys, Phys. Rev. B **102**, 094438 (2020).
[43] L. Zhu, D. C. Ralph, and R. A. Buhrman, Highly efficient spin-current generation by the spin Hall effect in $Au_{1-x}Pt_x$, Phys. Rev. Appl. **10**, 031001(R) (2018).
[44] D. Qu, S. Y. Huang, G. Y. Guo, and C. L. Chien, Inverse spin Hall effect in Au_xTa_{1-x} alloy film, Phys. Rev. B **97**, 024402 (2018).
[45] B. Coester, G. D. H. Wong, Z. Xu, J. Tang, W. L. Gan, and W. S. Lew, Enhanced spin Hall conductivity in tungsten-copper alloy, J. Magn. Magn. Mater. **523**, 167545 (2021).
[46] A. Yagmur, S. Sumi, H. Awano, and K. Tanabe, Large inverse spin Hall effect in Co-Tb alloys due to spin seebeck effect, Phys. Rev. Appl. **14**, 064025 (2020).
[47] Y. Miura and K. Masuda, First-principles calculations on the spin anomalous Hall effect of ferromagnetic alloys, Phys. Rev. Mater. **5**, L101402 (2021).
[48] J. Kübler and C. Felser, Berry curvature and the anomalous Hall effect in Heusler compounds, Phys. Rev. B **85**, 012405 (2012).
[49] J. Noky, Y. Zhang, J. Gooth, C. Felser, and Y. Sun, Giant anomalous Hall and Nernst effect in magnetic cubic Heusler compounds, npj Comput. Mater. **6**, 77 (2020).
[50] K. Manna, L. Muechler, T.-H. Kao, R. Stinshoff, Y. Zhang, J. Gooth, N. Kumar, G. Kreiner, K. Koepernik, R. Car, J. Kübler, G. H. Fecher, C. Shekhar, Y. Sun, and C. Felser, From colossal to zero: Controlling the anomalous Hall effect in magnetic Heusler compounds via Berry curvature design, Phys. Rev. X **8**, 041045 (2018).
[51] G. Qu, K. Nakamura, and H. Hayashi, First principles investigation of anomalous Hall and spin Hall effects in ferromagnetic CoPt, J. Phys. Soc. Jpn. **90**, 024707 (2021).
[52] M. Gradhand, D. V. Fedorov, P. Zahn, and I. Mertig, Spin Hall angle versus spin diffusion length: Tailored by impurities, Phys. Rev. B **81**, 245109 (2010).
[53] P. He, L. Ma, Z. Shi, G. Y. Guo, J.-G. Zheng, Y. Xin, and S. M. Zhou, Chemical composition tuning of the anomalous Hall effect in isoelectronic $L1_0FePd_{1-x}Pt_x$ alloy films, Phys. Rev. Lett. **109**, 066402 (2012).
[54] A.-M. Pradiotp and K. Nakamura, Slater-Pauling-like behavior of spin Hall conductivity in Pt-based superlattices, J. Math. Fund. Sci. **53**, 369 (2021).
[55] Y. Saito, N. Tezuka, S. Ikeda, and T. Endoh, W thickness dependence of spin Hall effect for (W/Hf)-multilayer electrode/CoFeB/MgO systems with flat and highly (100) oriented MgO layer, AIP Adv. **11**, 025007 (2021).
[56] C. Fang, C. H. Wan, Z. H. Yuan, L. Huang, X. Zhang, H. Wu, Q. T. Zhang, and X. F. Han, Scaling relation between anomalous Nernst and Hall effect in $[Pt/Co]_n$ multilayers, Phys. Rev. B **93**, 054420 (2016).
[57] T. Moriyama, Y. Shiratsuchi, T. Iino, H. Aono, M. Suzuki, T. Nakamura, Y. Kotani, R. Nakatani, K. Nakamura, and T. Ono, Giant anomalous Hall conductivity at the Pt/Cr_2O_3 interface, Phys. Rev. Appl. **13**, 034052 (2020).
[58] Z. B. Guo, W. B. Mi, R. O. Aboljadayel, B. Zhang, Q. Zhang, P. G. Barba, A. Manchon, and X. X. Zhang, Effects of surface and interface scattering on anomalous Hall effect in Co/Pd multilayers, Phys. Rev. B **86**, 104433 (2012).
[59] V. Keskin, B. Aktaş, J. Schmalhorst, G. Reiss, H. Zhang, J. Weischenberg, and Y. Mokrousov, Temperature and Co thickness dependent sign change of the anomalous Hall effect in Co/Pd multilayers: An experimental and theoretical study, Appl. Phys. Lett. **102**, 022416 (2013).

[60] C. Guarcello and F. S. Bergeret, Cryogenic memory element based on an anomalous Josephson junction, Phys. Rev. Appl. **13**, 034012 (2020).

[61] L. Salemi, M. Berritta, and P. M. Oppeneer, Quantitative comparison of electrically induced spin and orbital polarizations in heavy-metal/3*d*-metal bilayers, Phys. Rev. Mater. **5**, 074407 (2021).

[62] T. Taniguchi, J. Grollier, and M. D. Stiles, Spin-transfer torques generated by the anomalous Hall effect and anisotropic magnetoresistance, Phys. Rev. Appl. **3**, 044001 (2015).

[63] T. Seki, S. Iihama, T. Taniguchi, and K. Takanashi, Large spin anomalous Hall effect in $L1_0$ FePt: Symmetry and magnetization switching, Phys. Rev. B **100**, 144427 (2019).

[64] E. Wimmer, H. Krakauer, M. Weinert, and A. J. Freeman, Full-potential self-consistent linearized-augmented-plane-wave method for calculating the electronic structure of molecules and surfaces: O_2 molecule, Phys. Rev. B **24**, 864 (1981).

[65] M. Weinert, E. Wimmer, and A. J. Freeman, Total-energy all-electron density functional method for bulk solids and surfaces, Phys. Rev. B **26**, 4571 (1982).

[66] K. Nakamura, T. Ito, A. J. Freeman, L. Zhong, and J. Fernandez-de-Castro, Enhancement of magnetocrystalline anisotropy in ferromagnetic Fe films by intra-atomic noncollinear magnetism, Phys. Rev. B **67**, 014420 (2003).

[67] J. P. Perdew, K. Burke, and M. Ernzerhof, Generalized gradient approximation made simple, Phys. Rev. Lett. **77**, 3865 (1996).

[68] R. Yu, D. Singh, and H. Krakauer, All-electron and pseudopotential force calculations using the linearized-augmented-plane-wave method, Phys. Rev. B **43**, 6411 (1991).

[69] C. Li, A. J. Freeman, H. J. F. Jansen, and C. L. Fu, Magnetic anisotropy in low-dimensional ferromagnetic systems: Fe monolayers on Ag(001), Au(001), and Pd(001) substrates, Phys. Rev. B **42**, 5433 (1990).

[70] R. Wu and A. Freeman, Spin-orbit induced magnetic phenomena in bulk metals and their surfaces and interfaces, J. Magn. Magn. Mater. **200**, 498 (1999).

[71] W. Feng, Y. Yao, W. Zhu, J. Zhou, W. Yao, and D. Xiao, Intrinsic spin Hall effect in monolayers of group-VI dichalcogenides: A first-principles study, Phys. Rev. B **86**, 165108 (2012).

[72] L. Matthes, S. Küfner, J. Furthmüller, and F. Bechstedt, Intrinsic spin Hall conductivity in one-, two-, and three-dimensional trivial and topological systems, Phys. Rev. B **94**, 085410 (2016).

[73] J. Zhou and J.-C. Charlier, Controllable spin current in van der Waals ferromagnet Fe_3GeTe_2, Phys. Rev. Rese. **3**, L042033 (2021).

[74] W. Zhang, M. B. Jungfleisch, W. Jiang, Y. Liu, J. E. Pearson, S. G. E. te Velthuis, A. Hoffmann, F. Freimuth, and Y. Mokrousov, Reduced spin-Hall effects from magnetic proximity, Phys. Rev. B **91**, 115316 (2015).

[75] As an example, the film-FLAPW calculations were performed for Co_m/Pt_n heterostructure where the Co thickness (m) was varied from 1ML to 4ML while the Pt thickness (n) was fixed to 9ML. The spin magnetic moments of the Co (Pt) atomic layer at the interface are 2.08 (0.40), 1.98 (0.32), 1.97 (0.35), and 1.96 (0.32) μ_B for $m = 1$, 2, 3, and 4, respectively. The variation of spin magnetic moment with Co thickness is $\sim 0.1\mu_B$ for both the Co and Pt, which would not have a significant effect on the AHC.

[76] L. Zhu, D. C. Ralph, and R. A. Buhrman, Spin-orbit torques in heavy-metal-ferromagnet bilayers with varying strengths of interfacial spin-orbit coupling, Phys. Rev. Lett. **122**, 077201 (2019).